BNL-229619-2026-JAAM

Optimized manufacturing process for multilayer two-dimensional focusing mirrors in laboratory X-ray applications

T. Wang

To be published in "Journal of Manufacturing Processes"

May 2026

Photon Sciences

Brookhaven National Laboratory

U.S. Department of Energy

USDOE Office of Science (SC), Basic Energy Sciences (BES). Scientific User Facilities (SUF)

DISCLAIMER

Graphical Abstract

Optimized Manufacturing Process for Multilayer Two-Dimensional Focusing Mirrors in Laboratory X-ray Applications

Tianyi Wang, Mingda Lyu, Lei Huang, Brian Clarkston, Bonglea Kim, Yuriy Platonov, Nick Grupido, Licai Jiang, Corey Austin, Mourad Idir

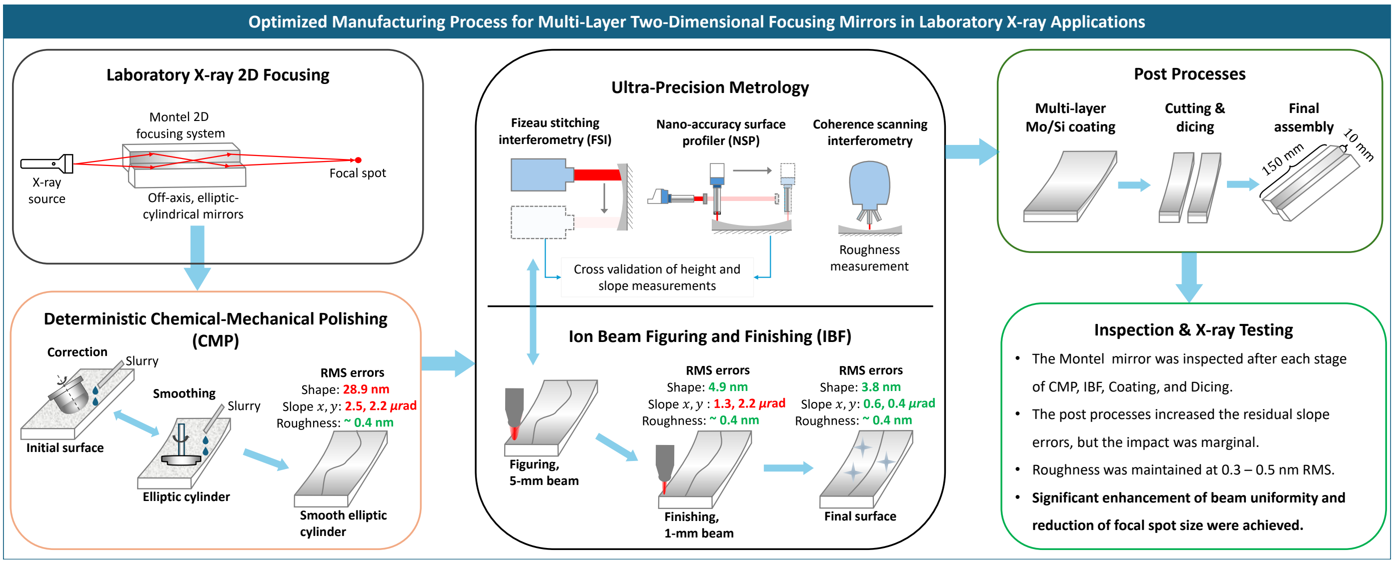

Highlights

Optimized Manufacturing Process for Multilayer Two-Dimensional Focusing Mirrors in Laboratory X-ray Applications

Tianyi Wang, Mingda Lyu, Lei Huang, Brian Clarkston, Bonglea Kim, Yuriy Platonov, Nick Grupido, Licai Jiang, Corey Austin, Mourad Idir

- Development of a complete Montel mirror manufacturing process.
- Process efficiency enhancement through chemo-mechanical polishing.
- Successful combination of advanced metrology and ion beam figuring for a 6-mrad Montel mirror.
- Multilayer coating, dicing, and gluing did not seriously affect the surface quality.
- Significant improvement in beam uniformity and reduction of focal spot size.

Optimized Manufacturing Process for Multilayer Two-Dimensional Focusing Mirrors in Laboratory X-ray Applications

Tianyi Wang[a,1,*], Mingda Lyu[b,1,**], Lei Huang[a,1], Brian Clarkston[b], Bonglea Kim[b], Yuriy Platonov[b], Nick Grupido[b], Licai Jiang[b], Corey Austin[a], Mourad Idir[a]

[a] *National Synchrotron Light Source II (NSLS-II), Brookhaven National Laboratory, PO Box 5000, Upton, 11973, New York, USA*
[b] *Rigaku Innovative Technologies, 1900 Taylor Rd, Auburn Hills, MI, 48326, USA*

Abstract

Recent advances in laboratory X-ray applications require high-performance optical components that achieve exceptional imaging resolution and beam uniformity within compact experimental setups. Montel mirrors have become a preferred solution due to their unique dual-reflection focusing mechanism and a space-efficient design. In this study, we present effective manufacturing process for producing Montel mirrors tailored to focus laboratory X-ray beams. The mirrors were fabricated from single-crystal silicon substrates, chosen for their high mechanical stability and compatibility with precision polishing techniques. Our approach begins with the integration of a deterministic chemo-mechanical polishing (CMP)-based pre-shaping step followed by ion beam figuring (IBF), significantly improving manufacturing efficiency. Subsequently, our custom-developed advanced metrology and IBF techniques were employed for fabricating an off-axis, elliptical cylinder Montel mirror system with a 6-mrad total slope, with stringent optical specifications. While post-IBF processes, including multilayer coating, dicing, and gluing, introduced minor surface errors, their impact on performance remained negligible. The Montel mirrors manufactured with the optimized process exhibited significantly improved beam uniformity and a reduced focal spot size. These findings validate our approach as a viable solution for high-precision Montel mirror fabrication and facilitate further advancements in laboratory X-ray applications.

Keywords: Montel mirror, ion beam figuring, chemo-mechanical polishing, high-efficiency fabrication, X-ray optics

1. Introduction

Laboratory X-ray beams are indispensable in material science, biology, and nanotechnology [1, 2]. Techniques such as X-ray diffraction (XRD [3], small-angle X-ray scattering (SAXS) [2], and X-ray fluorescence (XRF) [4] provide critical insights into the structural and compositional properties of materials at the atomic and molecular levels. The advancement of these applications requires high-performance optical components capable of manipulating and efficiently transporting X-ray beams within compact experimental setups.

In X-ray focusing optics, the elliptical focusing mechanism is widely employed, as illustrated in Fig. 1(a). Ideally, a single ellipsoidal mirror would provide the required two-dimensional (2D) focusing for high-resolution imaging and effective beam transport. However, fabricating a monolithic ellipsoidal mirror with nanometer-scale figure accuracy and sub-μrad slope error remains a significant challenge. To address this, alternative designs approximate the ideal ellipsoidal geometry using two elliptical cylinder mirrors. Among these, the Kirkpatrick-Baez (KB) system and the Montel mirror configuration [5], schematically depicted in Fig. 1(b), have emerged as practical solutions.

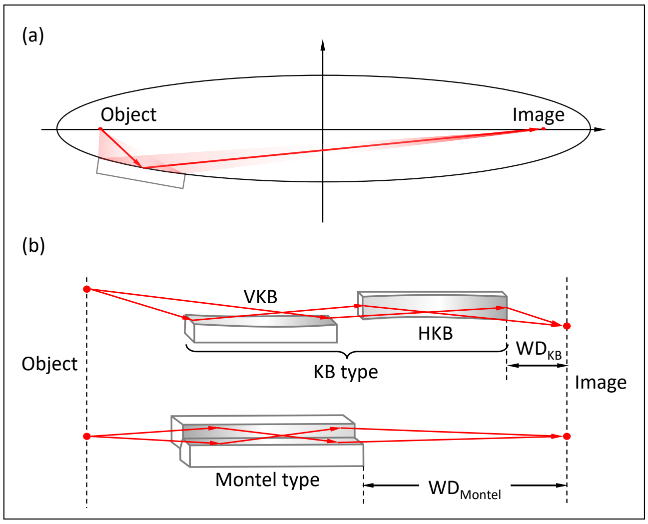

Figure 1: Schematics of (a) the off-axis elliptical focusing mechanism and (b) the Montel- and Kirkpatrick-Baez (KB)-type 2D X-ray focusing systems. The KB setup uses a vertical focusing mirror (VKB) and a horizontal focusing mirror (HKB) with different elliptical parameters, while the Montel setup features two perpendicular mirrors sharing identical elliptical parameters. Due to its compact design, the Montel system offers a longer working distance (WD) compared to the KB system and provides the same demagnification in both dimensions.

In a KB system, two independently fabricated elliptical mirrors, one for vertical focusing (VKB) and the other for horizon-

*Corresponding author
**Corresponding author
Email addresses: tianyi@bnl.gov (Tianyi Wang), mingda.lyu@rigaku.com (Mingda Lyu)
[1] These authors contribute equally.

tal focusing (HKB), are aligned orthogonally. In contrast, Montel mirrors use a nested arrangement of two identical elliptical mirrors to achieve 2D focusing. This integrated design offers three advantages:

- **Space Efficiency:** The nested configuration increases the effective WD, which is particularly beneficial in space-constrained laboratory environments.
- **Simplified Alignment:** The use of two identical mirrors reduces alignment complexities compared to KB systems, where independently fabricated mirrors require precise positioning.
- **Uniform Optical Parameters:** The symmetry of the Montel system ensures uniform focusing properties in both directions, enhancing beam uniformity and minimizing optical aberrations.

It is also worth mentioning that Montel mirrors have been successfully deployed in synchrotron radiation applications [6, 7]. Through precise optical adjustment, they have enabled diffraction-limited focal spots [8] and achieved a 50-nm resolution nano probe [9] at hard X-ray endstations.

Despite these advantages, the precise and efficient manufacturing of Montel mirrors remains a significant challenge. Existing studies offer few viable solutions [6], particularly when extending applications to the soft X-ray regime. As photon energy decreases, the required optical curvature increases, leading to additional complexities in metrology. Standard surface characterization techniques often fail to provide accurate and repeatable measurements at these higher curvatures without more advanced control and careful calibration.

In this work, as illustrated in Fig. 2(a), we present a comprehensive manufacturing process for Montel mirrors that integrates a deterministic chemo-mechanical polishing (CMP) preshaping step into the ion beam figuring (IBF) workflow. This integration significantly improves efficiency while achieving surface roughness below 0.4 nm root mean square (RMS). Subsequently, as shown in Figs. 2(b) and 2(c), we employed advanced metrology and IBF techniques to fabricate an off-axis, elliptical cylinder Montel mirror system with a 6-mrad total slope and a radius of curvature (RoC) ranging from 10.3 m to 49.2 m. Our Fizeau stitching interferometry (FSI) system provides feedback to the IBF processes. The nano-accuracy surface profiler (NSP) was used to cross-validate the FSI-measured data. A Zygo NewView coherence scanning interferometer was used to monitor the roughness evaluations. Post-processing steps (Fig. 2(d)), including multilayer Mo/Si coating, dicing, and gluing, introduced minor surface errors and their impact on performance was minimal. Ultimately, the optimized manufacturing process achieved RMS shape, slope, and roughness errors of 3.86 nm, 0.6 μrad, and 0.4 nm, respectively, which achieved the target RMS error specifications given in Fig. 2(e), leading to significant improvements in beam uniformity and a reduced focal spot size.

The rest of this paper is organized as follows. Section 2 introduces the specifications of the Montel mirrors. Section 3 details the fabrication and metrology techniques employed. The experimental results and X-ray performance evaluation of the fabricated mirrors are presented in Section 4. In Section 5, we discuss the broader implications of our findings for X-ray optical metrology and fabrication. Finally, Section 6 concludes the paper with a summary of our contributions and directions for future research.

2. Specifications of the Montel Mirrors

Figure 3(a) shows an ellipse centered at the origin of the canonical coordinate system, $(x_c, z_c) = (0, 0)$. The standard ellipse equation is given by

$$\frac{x_c^2}{a^2} + \frac{z_c^2}{b^2} = 1, \tag{1}$$

where a and b denote the semi-major and semi-minor axes, aligned with the beam propagation (x_c) and transverse (z_c) directions, respectively. In an ideal optical system, every ray emanating from the object is reflected precisely to the image point. For off-axis ellipses, an additional parameter, the off-axis distance (OAD), x_{OAD}, defines the lateral displacement of the mirror center from the origin along x_c.

In grazing-incidence X-ray optics, however, the system is more practically described by the object distance p, the image distance q, and the central grazing angle θ (see Fig. 3(a)), since these parameters directly relate to optical performance [10]. To facilitate mirror fabrication, a local mirror-centered coordinate system (x, z) is introduced with the mirror center positioned at x_0. The transformation from the canonical ellipse parameters (a, b, x_{OAD}) to the design parameters (p, q, θ) is expressed as:

$$\begin{aligned} p &= a + \frac{x_{\text{OAD}}\ \sqrt{a^2 - b^2}}{a}, \\ q &= a - \frac{x_{\text{OAD}}\ \sqrt{a^2 - b^2}}{a}, \\ \theta &= \arcsin\left(b\ \sqrt{\frac{a^2}{a^4 - (a^2 - b^2)x_{\text{OAD}}^2}} \right). \end{aligned} \tag{2}$$

The off-axis elliptical cylinder mirror surface in the mirror-centered coordinate system (with the ellipse oriented along the x-axis), $z_e\,(x, y)$, is described by

$$\begin{aligned} z_e(x, y) = z_0 &+ \chi \cdot (x - x_o) + \psi \cdot y \\ &+ \frac{(p+q)\sin\theta}{4pq + h^2}\Big[2pq - hx \\ &\qquad - 2\sqrt{pq}\ \sqrt{pq - hx - (x - x_o)^2} \Big]. \end{aligned} \tag{3}$$

Here, z_0, χ and ψ are the piston, pitch angle and roll angle, respectively, and $h = (p - q)\cos\theta$. A key advantage of this mirror-centered description is that it enables fine-tuning of z_0, χ and ψ to minimize the overall material removal during fabrication. Moreover, if small adjustments to θ and x_0 are acceptable—which is usually the case—the effective curvature can also be optimized. This approach not only reduces the material

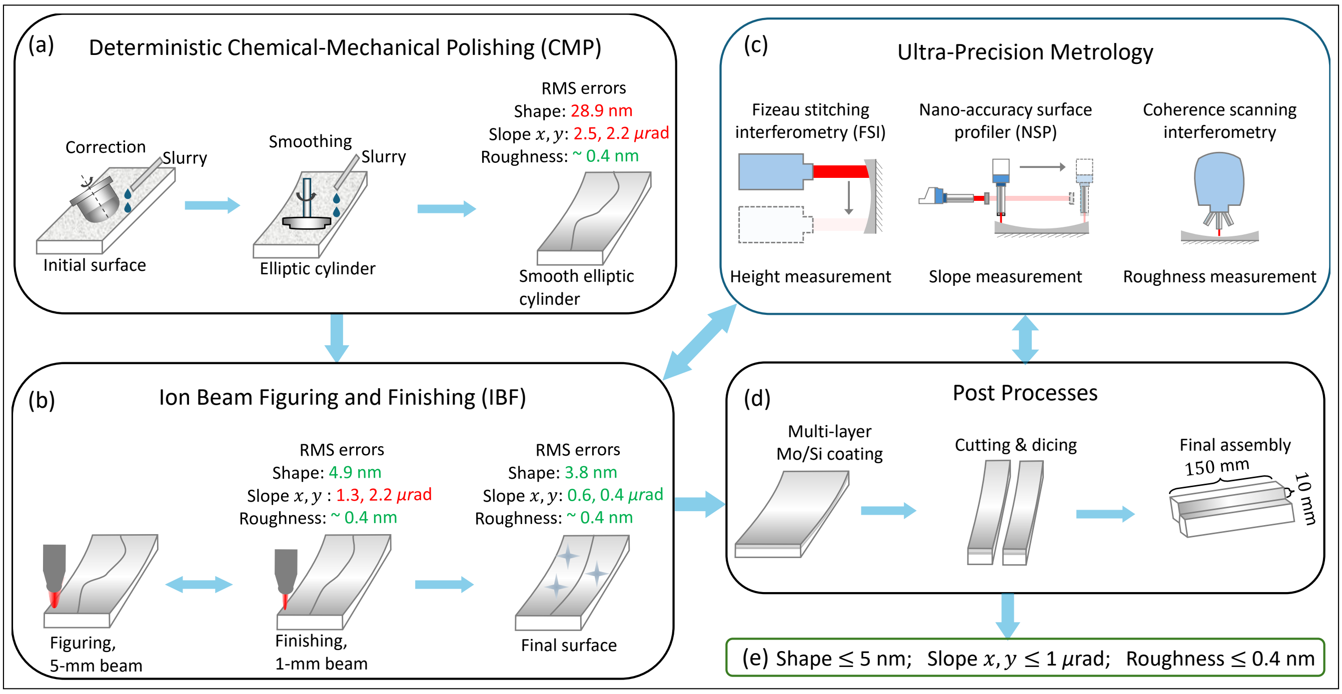

Figure 2: Schematic representation of the fabrication and metrology process for ultra-precise X-ray mirrors. (a) The process begins with deterministic chemical-mechanical polishing (CMP), which pre-shapes the surface into an elliptical cylinder while reducing errors in shape, slope, and roughness. (b) Next, ion beam figuring and finishing (IBF) further refines the surface to achieve the required nanometer-scale accuracy. (c) Throughout the fabrication process, ultra-precision metrology techniques, including Fizeau stitching interferometry (FSI), nano-accuracy surface profiler (NSP), and coherence scanning interferometry, are employed for height, slope, and roughness measurements. (d) Finally, post processes such as multilayer Mo/Si coating, cutting, and assembly are performed to prepare the mirror for application. The ultra-precision metrology techniques in (c) are applied again to post-coating and dicing. (e) The target residual RMS errors are shape error ≤ 5 nm, slope $x, y \leq 1$ μrad, and roughness ≤ 0.4 nm.

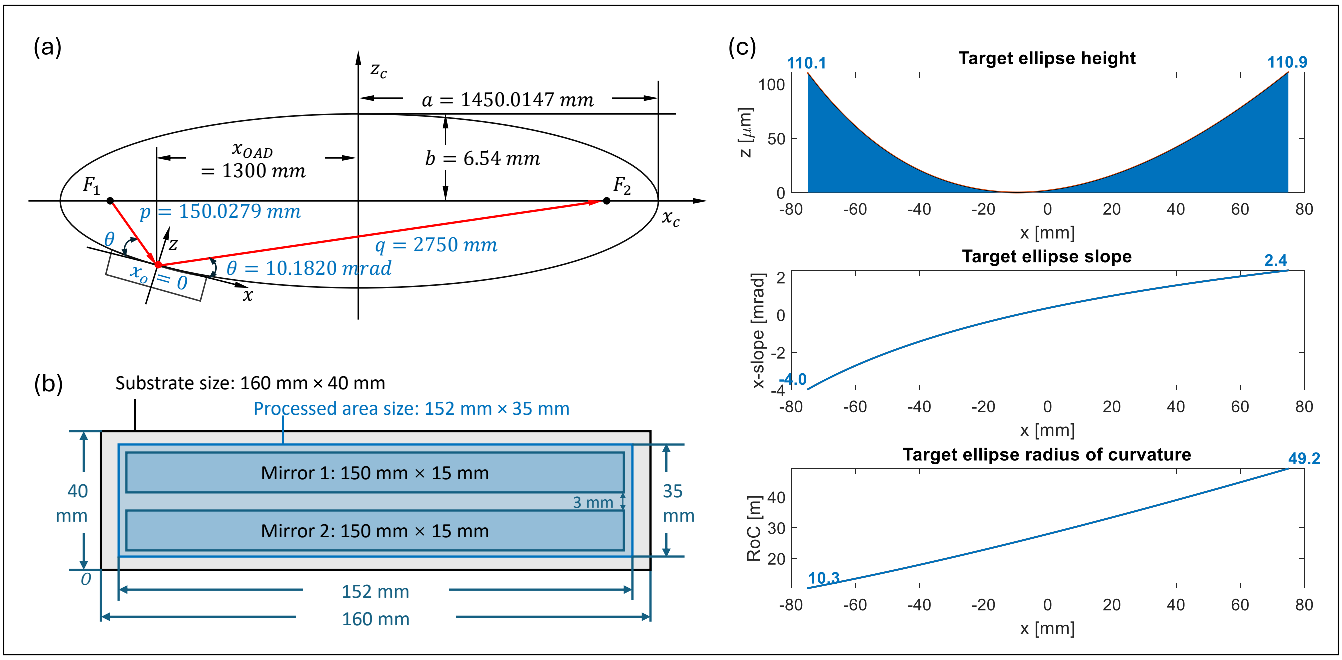

Figure 3: Schematics of (a) the design parameters of the target off-axis ellipse of the Montel mirrors, (b) the mirror substrate dimensions, and (c) the height, slope and radius of curvature (RoC) calculated using Eq. (3).

removal but also facilitates cross-validation between different metrology instruments, as curvature is always hard to be accurately measured.

The Montel mirrors in this study are designed with the following parameters of $p = 150.0279$ mm, $q = 2750$ mm, and $\theta = 10.1820$ mrad. The mirrors were fabricated on a single-crystal silicon substrate. As shown in Fig. 3(b), the substrate measures 160 mm × 40 mm, with a processed area of 152 mm × 35 mm, which is the area fabricated as a single piece with the same design parameters. A 3-mm central region is reserved as a cutting zone, after which each mirror of the Montel system is trimmed to a final size of 150 mm × 15 mm. The two mirror segments are then diced and orthogonally bonded together.

As shown in Fig. 3(c), the height, slope, and RoC profiles along the x-axis are generated using Eq. (3) with $\chi = \psi = 0$. Notably, the total slope variation exceeds 6.4 mrad and the minimum RoC is as small as 10.2 m. The RMS height and slope errors are required to be less than 5 nm and 1 μrad, respectively, which pose significant challenges for precision metrology.

3. Metrology and fabrication of the Montel mirrors

In our previous work on using IBF to fabricate elliptical hard X-ray mirrors, we typically began with spherical mirrors with the best-fit RoC as the base geometry. This approach leveraged conventional pitch polishing ability to achieve sub-0.3 nm RMS roughness [11, 12]. Particularly, the deviation from sphericity of hard X-ray KB mirrors from the best-fit spherical mirrors is typically small, with the slope variation along the x-dimension on the order of approximately ∼1 mrad. In these cases, the average material removal was on the order of microns, and the total dwell time ranged from several hours to tens of hours—both within acceptable limits.

However, when the total slope variation is large (6.2 mrad in this study) and the mirror length increases (152 mm in this study), the departure from the best-fit spherical mirror becomes significant, drastically impacting processing efficiency. This effect is illustrated in Fig. 4(a), which presents the desired removal and dwell time maps for shaping the target elliptical cylinder mirror (Fig. 3) from the best-fit spherical mirror using the tool influence function (TIF) shown in Fig. 6(a). The best-fit RoC is 25.83 m. With this IBF TIF, the estimated processing time to achieve the target shape is approximately 10 days. This IBF run is impractical, as a single pass over such a long duration would not yield a convergent surface finish.

Starting from a cylindrical mirror, as shown in Fig. 4(b), where the y-dimension is already flat, reduces the required material removal compared to the spherical case. However, the total processing time remains nearly 8 days, making this approach similarly inefficient. Therefore, as mentioned in Fig. 2, we proposed integrating a deterministic CMP process prior to IBF to simultaneously pre-shape the elliptical cylinder mirror surface and maintain sub-0.3 nm RMS roughness. After CMP, IBF was applied using a 5-mm beam for figuring and a 1-mm beam for finishing. Finally, multilayer Mo/Si coating, dicing, and final assembly were performed to complete the Montel system. The following sections provide details of each processing step shown in Fig. 2.

3.1. *Pre-shaping with deterministic chemical-mechanical polishing (CMP)*

Deterministic CMP is a hybrid material removal process that integrates chemical etching with mechanical abrasion to achieve

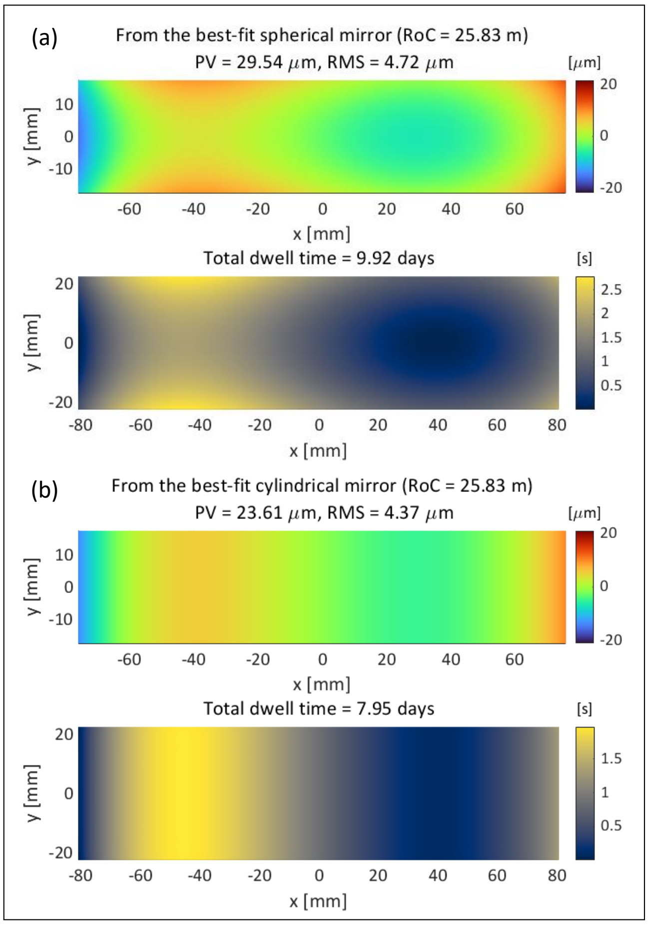

Figure 4: Residual height error and dwell time maps for the IBF process, starting from (a) the best-fit spherical mirror, (b) the best-fit cylindrical mirror, and (c) the CMP-pre-shaped elliptical-cylindrical mirror, to achieve the target elliptical-cylindrical mirror. The best-fit radius of curvature (RoC) is 25.83 m.

ultra-precise surface shaping while maintaining excellent surface smoothness. Unlike traditional mechanical polishing, CMP uses chemical reactions to soften the material, enabling controlled removal with minimal subsurface damage. This makes it especially effective for large-scale figure correction (spatial frequency lower than 4 mm^{-1}) while preserving nanoscale roughness, making it an ideal pre-shaping technique for producing high-precision X-ray optics using IBF.

As shown in Fig. 2(a), the CMP pre-shaping process involves two main steps: correction and smoothing. During the correction step, low-frequency figure errors were addressed by selectively removing material to shape the mirror surface toward the desired elliptical cylinder profile. This was done using a 7-axis CNC optical polishing machine with a cerium oxide slurry recirculated through a filtration system. A bonnet-style tool fitted with polyurethane polishing pads in radii of 40 mm, 10 mm, and 5 mm was used progressively from coarse to fine polishing, respectively. These flexible tools conformed to the local surface curvature, enabling precise material removal. The tool operated at a 20° inclination and a rotational speed of 2000 rpm, under controlled pressure ranging from 150 N to 30 N. This setup allowed for accurate correction of large-scale shape deviations while minimizing subsurface damage. To optimize error convergence, dwell time and feed velocity were carefully adjusted based on metrology feedback from a multi-wavelength interferometer. Through iterative cycles of deterministic correction and measurement, optimal low spatial frequency figure error was achieved. Figure 5(a) displays the residual height error of the CMP-processed mirror surface, as measured by the interferometer. CMP effectively reduces the initial figure error to 23.78 nm RMS, representing a two-order-of-magnitude improvement compared to mirrors initially shaped as spherical or cylindrical, as shown in Fig. 4.

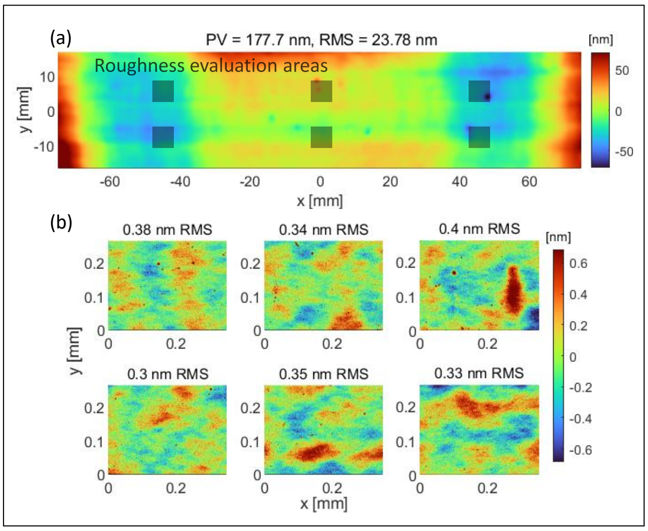

Figure 5: (a) The residual height error after CMP achieves 23.78 nm RMS, as measured by the multiwavelength interferometer. (b) Surface roughness across all evaluation areas is ≤ 0.4 nm RMS.

After figure correction, the smoothing step eliminates mid-to-high spatial frequency errors and achieves ultra-smooth surface roughness. The smoothing was performed using the same 7-axis CNC optical polishing machine with a colloidal silica slurry recirculated through a filtration system. A flat tool fitted with polyurethane or buffed polyurethane polishing pad with 15 mm in diameter, was used progressively from initial to fine smoothing. The tool operated in normal contact mode at 2000 rpm, under a constant pressure of 100 N and a constant feed velocity of 200 or 400 mm/min. The polishing pad evenly distributed pressure across the surface, effectively reducing micro-scratches and residual texture from the correction step. Surface roughness is monitored using the Zygo NewView coherence scanning white light interferometer to ensure the final roughness meets the stringent standards for high-performance X-ray optics. Through iterative cycles of non-deterministic smoothing and measurement, optimal mid-to-high spatial frequency errors were achieved. Figure 5(b) shows the roughness values measured in six evaluation areas using a 20× objective on the Zygo NewView. All values are below 0.4 nm RMS, highlighting that the integration of the correction and smoothing steps in the CMP process significantly enhances fabrication while maintaining ultra-low RMS roughness.

3.2. *Low-Frequency Error Correction with a 5-mm ion beam*

To further reduce residual errors beyond what is achievable with deterministic CMP, a more precise fabrication technique is required. Ion beam figuring (IBF) was selected for this task due to its deterministic material removal capability, enabling precise shape correction at the sub-nanometer scale [12]. Our in-house developed IBF system equipped with a Kaufman & Robinson KDC10 ion source was adopted for this task. The ion source parameters used in the experiment were beam voltage = 600 V, beam current = 10 mA, accelerator voltage = -90 V, and accelerator current = 2 mA. A two-step IBF process was implemented: a 5-mm ion beam was used for global figure correction, followed by a 1-mm ion beam for fine surface finishing. The beam size was controlled by a pinhole system in front of the ion source. Figure 6 illustrates the two ion beam sizes used in the process.

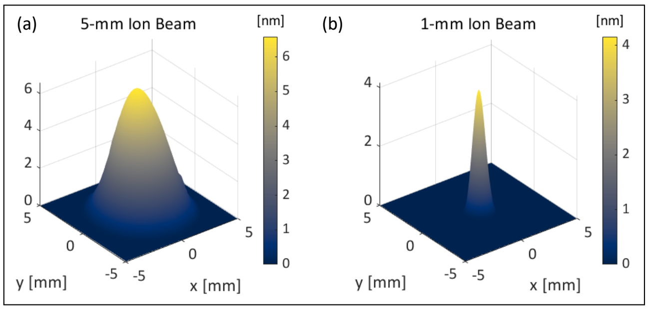

Figure 6: Schematic of the IBF process using (a) a 5-mm beam for global figure correction and (b) a 1-mm beam for fine finishing.

IBF relies on ultra-precision metrology feedback to ensure high predictability. For this purpose, we employed our in-house developed FSI platform [13, 14]. To obtain reliable measurements in each FSI subset, a small number of fringes is required. As illustrated in Fig. 7(a), we used an 8.4 mm × 37.3 mm subset size with a 90% overlap between consecutive subsets. A total of 183 subsets were acquired in a single FSI run, and the stitched residual height error map is shown in Fig. 7(b). Compared to the multiwavelength interferometer measurement in Fig. 5(a), FSI reveals the same overall error trend with a smaller RMS error, which requires further validation of the measurement results.

Our FSI system has previously demonstrated a repeatability of 0.3 nm RMS when measuring flat or near-flat optical surfaces [14, 12]. However, the mirror in this study exhibits a total slope variation of 6 mrad (see Fig. 3(c)), necessitating verification of FSI's reliability under such conditions. To assess its accuracy, we employed our in-house developed NSP system [15, 16] for cross-validation, as depicted in Fig. 2(c).

The NSP operates on the principle of deflectometry, utilizing two high-precision autocollimators to assess surface slopes with nanoradian sensitivity. The measuring autocollimator directs a collimated light beam onto the surface under test and detects the angle of the reflected beam. By scanning across the surface, it measures local slope variations. Simultaneously, the reference autocollimator monitors a stable reference beam,

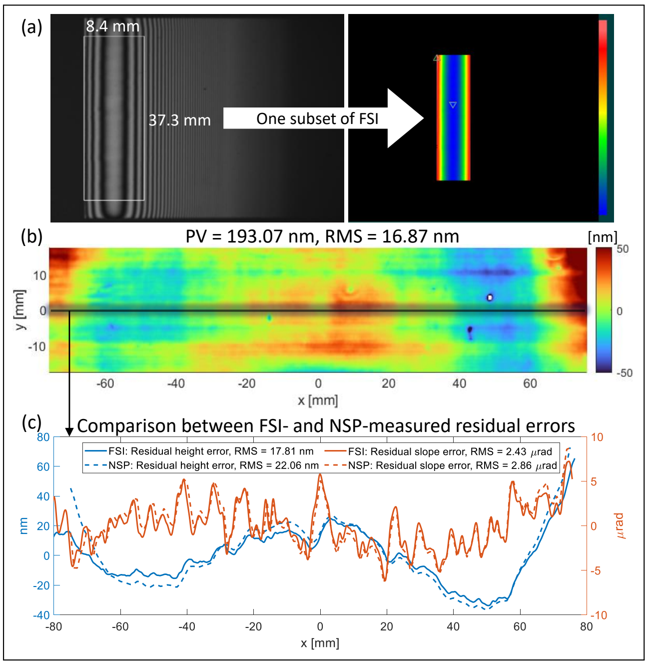

Figure 7: Fizeau stitching interferometry (FSI) provides metrology feedback for the ion beam figuring (IBF) process. (a) Each FSI subset covers an area of 8.4 mm × 37.3 mm. (b) The FSI-measured residual height error relative to the target elliptical cylinder surface is 28.87 nm RMS. (c) The central line of the FSI error map is extracted and compared with measurements from the nano-accuracy surface profiler (NSP), showing strong agreement.

enabling the system to compensate for environmental disturbances and systematic errors, thereby enhancing measurement reliability.

As NSP is a one-dimensional (1D) measuring instrument, as shown in Fig. 7(c), we compare the central-line residual errors measured by FSI and NSP. To align the data, we applied a 2.5 mm sliding window to the FSI height measurements, which matches the NSP's pupil size. The strong agreement between these two techniques, which are based on different measurement principles, confirms the reliability of FSI for characterizing high-slope X-ray mirrors.

Low-frequency error correction with IBF was first performed. A Gaussian low-pass filter with a cutoff frequency of 10 mm^{-1} was applied to the residual height error map in Fig. 7(b) to isolate the low-frequency component, which was then used for dwell time calculation. Figure 8(a) presents the IBF dwell time map used for correction with the 5-mm ion beam (see Fig. 6(a)), along with the corresponding estimated and measured residual height errors after processing. The dwell time was computed using our proposed universal dwell time optimization (UDO) method [17, 18], ensuring efficient material removal across the mirror surface. Once optimized, the dwell time was converted into precise scanning velocities along a raster tool path using our enhanced position-velocity-time (E-PVT) algorithm [19], which ensures smooth and deterministic beam motion during the IBF process. After a 44.69 min IBF process, the FSI-measured residual height error achieved 4.78 nm RMS, which confirms that IBF effectively reduced the low-frequency error to the specified level (i.e ≤ 5 nm RMS) while preserving overall surface integrity. Nonetheless, after converting the residual height map into residual slope maps, as illustrated in Fig. 2(b), we found that slope errors in the x and y dimensions were still out of specification. Therefore, further IBF processes are necessary.

3.3. Middle-frequency error correction with a 1-mm ion beam

Slope errors are more sensitive to middle-frequency surface deviations. Therefore, we focused on correcting only the middle-frequency components using the 1-mm ion beam shown in Fig. 6(b). Specifically, a Gaussian band-pass filter with cutoff frequencies of 10 mm^{-1} and 2 mm $^{-1}$ was applied to the measured residual height error in Fig. 8(a), and the resulting middle-frequency error map is demonstrated in Fig. 9, where the residual RMS error is 2.42 nm.

It is worth noting that precise positioning is critical when using small machine tools for finishing optical surfaces, as even a slight deviation in dwell positions can compromise the overall surface quality. Although positioning errors can be compensated for in subsequent steps [20, 12], it is preferable to ensure accurate positioning before the process begins. In our IBF system, two primary sources contribute to positioning errors: the coordinate correspondence between the IBF and FSI systems, and the misalignment caused by the rotation center issue in FSI.

The correspondence between the FSI and IBF coordinate frames can be easily established due to the Gaussian-like profile of the ion beam. As shown in Fig. 10, the 1-mm ion beam (Fig. 6(b)) was used to create multiple footprints in unprocessed areas of the mirror surface. The stage encoder readings of the centers of these Gaussian-like footprints were recorded for both the IBF and FSI systems. By comparing these readings, the coordinate correspondence between the two systems was accurately determined [12].

Resolving the rotation center issue in FSI, however, is not straightforward. When measuring each subset, the mirror must be rotated to null the fringes to maximally ensure sufficiently repeatable results [14]. Due to the varying dimensions of mirrors, establishing a consistent reference point in the mechanical design is challenging. This issue is less critical when measuring flat or near-flat optical surfaces, which the current FSI system was originally designed for.

To identify and compensate for potential alignment errors when measuring this 6-mrad slope variation mirror, we created two 1-mm ion beam footprints on opposite sides of the mirror surface, as illustrated in Fig. 10, and recorded the distances between them in both the FSI and IBF frames. The measurements revealed a 0.9869 mm discrepancy between the two distances, indicating that the FSI rotation center issue caused the measured length to be 0.6% longer than the actual mirror length. Consequently, the x coordinates of the FSI measurement data in Fig. 9 were adjusted by shrinking them by 0.6% to compensate for this error.

Figure 8(b) presents the dwell time map used for correcting the middle-frequency error shown in Fig. 9, along with the estimated and measured residual height errors after processing. After a 133.18 min IBF process, a strong agreement between the predicted and measured results was achieved, which validates the effectiveness of our positioning calibration strategy.

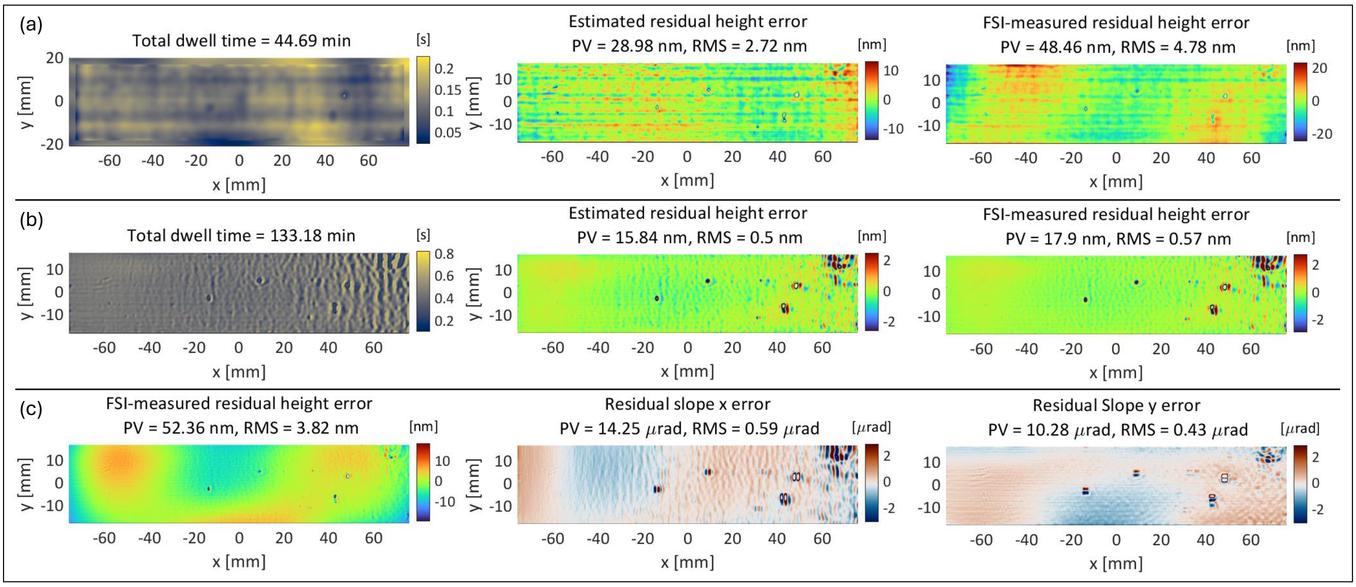

Figure 8: (a) Dwell time, estimated residual height error, and FSI-measured residual error for 5-mm ion beam correction of low-frequency errors. (b) Dwell time, estimated residual height error, and FSI-measured residual error for 1-mm ion beam correction of mid-frequency errors, characterized by applying a Gaussian band-pass filter with cutoff frequencies of 10 mm^{-1} and 2 mm $^{-1}$ (c) Final residual height and slope errors after the ion beam figuring and finishing processes, meeting the specifications outlined in Fig. 2(e).

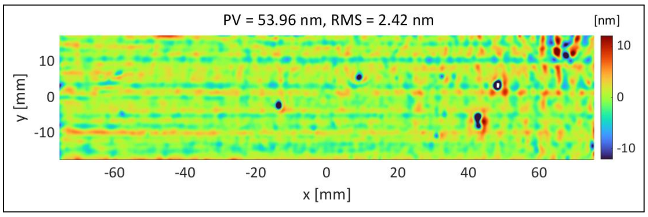

Figure 9: Residual middle-frequency error after applying a Gaussian band-pass filter with cutoff frequencies of 10 mm^{-1} and 2 mm $^{-1}$ to the FSI-measured residual height error in Fig. 8(a).

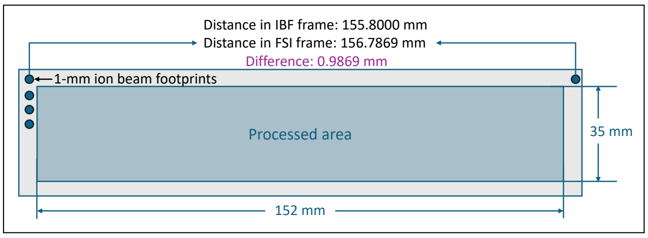

Figure 10: Positioning calibration between the Fizeau stitching interferometry and ion beam figuring systems.

The final result after the low- and middle-frequency corrections using IBF is demonstrated in Figure 8(c). The residual height error is 3.82 nm RMS, indicating a high degree of precision in the correction process. Slope errors were calculated using the same strategy outlined in Section 3.2, with a residual slope error of 0.59 μrad in the x dimension and 0.43 μrad in the y dimension. A detailed inspection of these slope errors is postponed until Section 3.4, which carefully compares the results before and after each post-processing step. Additionally, roughness was evaluated at the same areas shown in Fig. 11, and the IBF process successfully maintained the roughness throughout the correction.

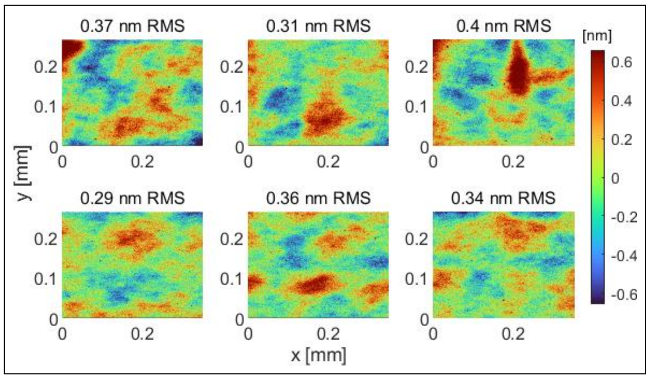

Figure 11: Surface roughness across all evaluation areas after IBF is maintained at ≤ 0.4 nm RMS.

3.4. Multilayer coating, dicing and final assembly

Following the IBF process, the Montel mirrors underwent multilayer Mo/Si coating, dicing, and final assembly to complete the fabrication, as shown in Fig. 2(d). The multilayer coating was performed by using a magnetron sputtering deposition system, with specially designed masks used to control the d-spacing with the required precision. X-ray reflectometry measurements (Figure 12) confirmed the accuracy of the mutilayer period, showing an d-spacing deviation of 0.0165 Å RMS. The associated reflectivity loss due to d-spacing errors was 0.02%, resulting in an average surface reflectivity of 68%. Precision dicing and orthogonal optical assembly were achieved using a CNC dicing machine and custom-designed alignment tools.

The impact of each step on surface quality was carefully evaluated using NSP measurements of residual slope errors.

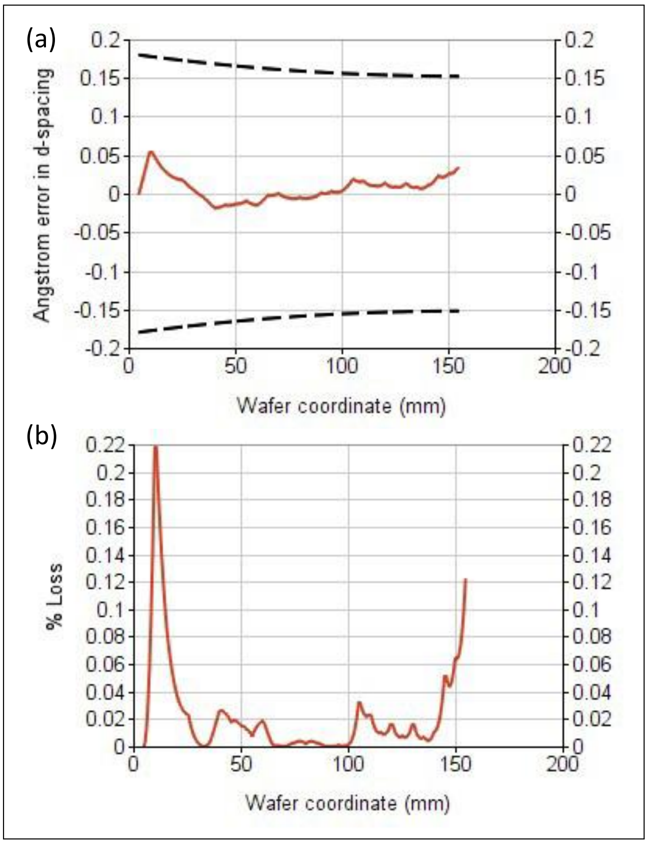

Figure 12: X-ray reflectivity measurements after multilayer coating. (a) Deviation of the multilayer d-spacing from the designed value. (b) Impact of d-spacing error on multilayer reflectivity loss.

Figure 13 illustrates the analysis of residual slope errors at different processing stages. In Fig. 13(a), Mirror 1 and Mirror 2 are displayed, with their respective center lines highlighted in blue and red. These lines were measured using NSP to track residual slope errors after IBF, after coating, and after dicing. Figures 13(b) and 13(c) present the NSP-measured slope errors along the blue (Mirror 1) and red (Mirror 2) center lines, respectively, using different line and marker styles to distinguish the results at each processing stage.

For Mirror 1, the residual slope error was 0.43 μrad after IBF and remained nearly unchanged at 0.44 μrad after multilayer Mo/Si coating, thanks to our high-performance coating technique [21]. However, after dicing, the slope error increased to 0.81 μrad, indicating that dicing introduced additional surface distortions. Similarly, for Mirror 2, the slope error increased from 0.39 μrad after IBF to 0.51 μrad after coating, showing a slightly higher but still minor effect. After dicing, the slope error further increased to 0.75 μrad, which, while more significant, still remained at the ≤ 1 μrad specification. These results demonstrate that while dicing has a moderate impact on surface quality, its effect remains within an acceptable range for high-precision X-ray optics. Roughness measurements after coating and dicing are demonstrated in Fig. 14, which indicates that the post processes had little impact on roughness.

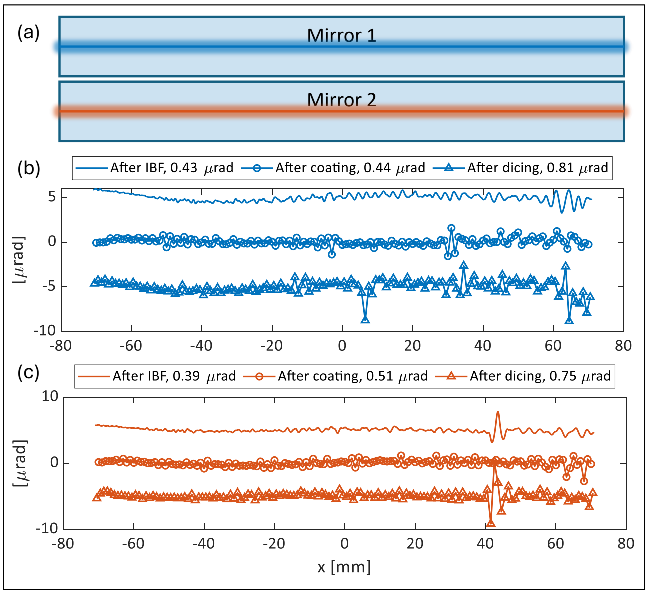

Figure 13: Impact of multilayer coating and dicing on residual slope errors. (a) Mirror 1 and Mirror 2 with center lines highlighted in blue and red. (b) NSP-measured slope errors along the blue line (Mirror 1) after IBF, after coating, and after dicing. (c) Same analysis as (b) but for the red line (Mirror 2).

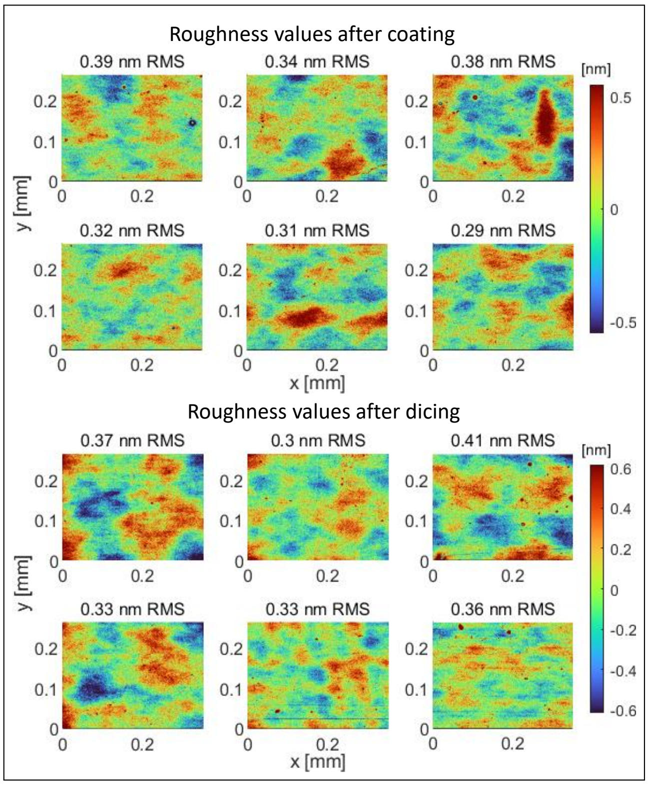

Figure 14: Surface roughness after the coating and dicing processes. These post processes had little impact on roughness.

4. Experimental result and performance evaluation

To assess the efficacy of our mirror manufacturing process, we conducted an X-ray performance evaluation using an in-house developed micro-focusing test bench. This system is designed to measure beam uniformity and focal spot size, providing a direct comparison of mirrors fabricated by different technologies or at different fabrication stages.

Figure 15 illustrates the X-ray intensity distributions and their vertical projections for mirrors. Figure 15(a) depicts the replication mirror, fabricated by depositing a multilayer coating on a flat silicon substrate, followed by stencil-based bending. The resulting focal spot dimensions are 350 μm (horizontal) and 340 μm (vertical). Notably, the intensity profile exhibits poor uniformity, as evidenced by irregularities in the vertical projection. This non-uniformity is attributed to surface errors arising from the stencil and imperfect wafer contact, leading to slope and height errors of 2 arcsec RMS and 50 nm RMS, respectively, for these optics.

In contrast to replication technology, the multilayer can be directly deposited on a prefigured substrate processed by polishing technologies, as demonstrated in the present study. Fig. 15(b) illustrates the enhanced X-ray performance achieved with a multilayer coating on a CMP-processed mirror. The focal spot size was measured to be 430 μm horizontally and 320 μm vertically. The beam uniformity showed noticeable enhancement compared to the replication mirror, but some inconsistencies remained in the intensity distribution.

Following IBF processing, the mirror achieved the best beam uniformity and the smallest focal spot size, as illustrated in Fig. 15(c). The final focal spot measured 350 μm in the horizontal direction and 250 μm in the vertical direction. The intensity projection demonstrated a well-distributed beam profile, confirming that IBF effectively minimized residual figure errors and improved focusing performance. The vertical focal spot distortion is primarily attributed to orthogonal alignment errors, not mirror surface quality.

X-ray performance evaluation demonstrates a progressive improvement in mirror quality across fabrication technologies or stages. The transition from replication mirrors to CMP-processed prefigured mirrors enhanced beam uniformity, which was further refined by IBF. These findings validate the proposed manufacturing process's ability to produce high-precision X-ray optics for demanding applications.

5. Discussion

The manufacturing process developed in this study integrates deterministic CMP as a pre-shaping step prior to IBF, significantly improving the efficiency of producing high-precision Montel mirrors for laboratory X-ray applications. CMP reduced the initial figure error to 16.87 nm RMS, as demonstrated in Figure 7(b), the subsequent IBF process requires substantially less material removal compared to conventional initial geometries, such as spherical or cylindrical mirrors (Fig. 4). This reduction reduced processing time from several days to a few hours, marking a notable advancement in the fabrication of two-dimensional (2D) focusing optics. The combination of CMP's large-scale figure correction and IBF's sub-nanometer precision enables the production of mirrors that meet stringent specifications, including shape errors $\leq$ 5 nm RMS, slope errors $\leq$ 1 μrad, and roughness $\leq$ 0.4 nm RMS.

Despite these advancements, certain limitations persist that require further exploration. The power spectral density (PSD) measurements before and after IBF, as shown in Fig. 16, suggest that the middle-frequency peaks that IBF struggles to eliminate originates from the correction step in CMP. A potential remedy lies in refining the CMP process through iterative correction and smoothing cycles. By applying multiple passes with adjusted dwell times and polishing parameters, it may be possible to target and reduce these frequency-specific deviations before IBF, thereby enhancing the overall surface quality.

Additionally, the surface roughness achieved, consistently $\leq$ 0.4 nm RMS across all evaluated areas (Figs. 5(b), 11 and 14), meets the required specifications for laboratory X-ray optics. However, the smoothing step in CMP, utilizing a damping pad, indicates that further improvements are feasible with extended smoothing times. This observation implies that the proposed strategy's capability exceeds the current requirements, offering flexibility for applications demanding even lower roughness, such as soft X-ray or synchrotron-grade optics.

Lastly, a critical design choice in this manufacturing process is the fabrication of both Montel mirrors on a single substrate prior to dicing. This approach ensures that the two mirrors share identical optical parameters, such as radius of curvature and surface figure, which is essential for their precise assembly and alignment in the Montel configuration. By processing the 152 mm × 35 mm substrate as a single unit before separating it into two 150 mm × 15 mm segments (Section 2), variations that could arise from fabricating the mirrors independently are minimized. This consistency simplifies the alignment process, reduces optical aberrations, and enhances beam uniformity, as evidenced by the X-ray performance results in Figure 15(c). The minor surface distortions introduced during dicing and coating, with slope errors increasing to 0.81 μrad and 0.75 μrad for Mirrors 1 and 2 respectively (Section 3.4), remain within the $\leq$ μrad specifications, further validating the efficacy of this strategy.

6. Concluding remarks and future work

This study demonstrates an optimized manufacturing process for Montel mirrors tailored to laboratory X-ray applications, achieving high precision and efficiency. By integrating deterministic chemo-mechanical polishing (CMP) with ion beam figuring (IBF), we fabricated mirrors with final residual errors of 3.82 nm RMS for shape, slope errors of 0.81 μrad and 0.75 μrad for the two mirrors after multilayer coating and dicing, and roughness of $\leq$ 0.4 nm RMS, all meeting the target specifications outlined in Figure 3(e). The X-ray performance evaluation (Section 4) confirms the process's efficacy, with the assembled Montel mirrors exhibiting a reduced focal spot size of 350 μm × 250 μm and significantly improved beam uniformity compared to earlier fabrication stages (Figure 15). These achievements validate the CMP-IBF approach as an effective solution for producing high-performance 2D focusing optics, addressing the demands of compact laboratory X-ray setups for applications such as X-ray diffraction, scattering, and fluorescence.

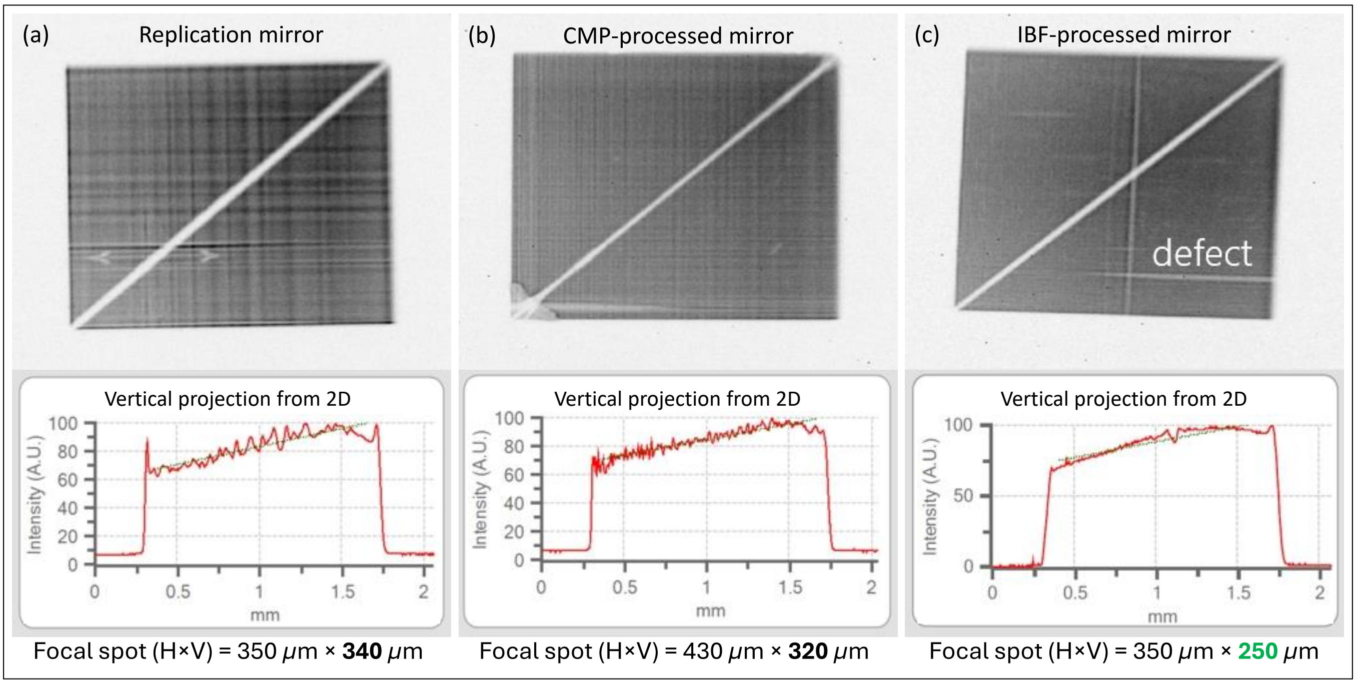

Figure 15: X-ray performance evaluation of mirrors at different fabrication stages. (a) X-ray intensity image and vertical projection for the replication mirror, showing a poor beam uniformity. (b) Results after the CMP process, where beam uniformity improves, and the focal spot size is reduced. (c) Results after IBF processing, achieving the best beam uniformity and a reduced focal spot size of 350 μm × 250 μm.

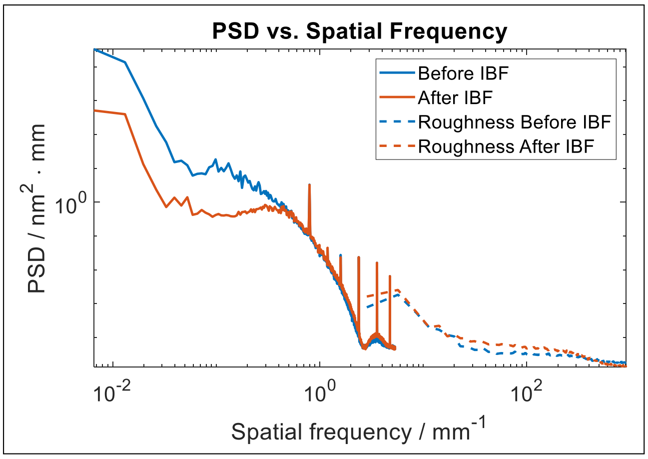

Figure 16: Power spectral density curves measured by FSI and Zygo NewView before and after ion beam figuring.

Future work will focus on addressing the limitations identified in Section 5 to further improve the process's capabilities, including implementing iterative correction and smoothing cycles and extending smoothing times in CMP to achieve even lower middle-to-high-frequency error levels.

This work establishes a robust foundation for Montel mirror fabrication, with clear directions for improvement. Future efforts will refine the CMP-IBF workflow, minimize post-process effects, and explore its applicability to more demanding X-ray optics, paving the way for advancements in both laboratory and synchrotron-based research.

CRediT authorship contribution statement

Tianyi Wang:Conceptualization, Methodology, Investigation, Software, Data curation, Funding acquisition, Writing - Original draft preparation. **Mingda Lyu**: Methodology, Investigation, Software, Data curation, Writing - Review and editing. **Lei Huang**: Validation, Formal analysis, Writing - Review and editing. **Brian Clarkston**: Investigation, Software, Data curation, Writing - Review and editing. **Bonglea Kim**: Supervision, Resources, Writing - Review and editing **Yuriy Platonov**: Supervision, Resources, Writing - Review and editing **Nick Grupido**: Supervision, Resources, Writing - Review and editing **Licai Jiang**: Project administration, Writing - Review and editing **Corey Austin**: Writing - Review and editing **Mourad Idir**: Project administration, Funding acquisition, Writing - Review and editing

Declaration of competing interest

The authors declare that they have no known competing financial interests or personal relationships that could have appeared to influence the work reported in this paper.

Acknowledgements

This work was supported by the Accelerator and Detector Research Program, part of the Scientific User Facility Division of the Basic Energy Science Office of the U.S. Department of Energy (DOE), under the Field Work Proposal No. FWP-PS032. This work was performed under the BNL LDRD Project 25-024 "DEMAND: Deterministic manufacturing of strongly curved diffraction-limited X-ray mirrors". This research was performed at the Optical Metrology Laboratory at the National Synchrotron Light Source II, a U.S. DOE Office of Science User Facility operated by Brookhaven National Laboratory (BNL) under the Contract No. DE-SC0012704.

References

[1] C. Y. Hémonnot, S. Köster, Imaging of biological materials and cells by X-ray scattering and diffraction, ACS nano 11 (9) (2017) 8542–8559.

[2] J. Bolze, V. Kogan, D. Beckers, M. Fransen, High-performance small- and wide-angle X-ray scattering (SAXS/WAXS) experiments on a multi-functional laboratory goniometer platform with easily exchangeable X-ray modules, Review of Scientific Instruments 89 (8) (2018).

[3] A. A. Bunaciu, E. G. UdriŞTioiu, H. Y. Aboul-Enein, X-ray diffraction: instrumentation and applications, Critical reviews in analytical chemistry 45 (4) (2015) 289–299.

[4] M. Haschke, J. Flock, M. Haller, X-ray fluorescence spectroscopy for laboratory applications, John Wiley & Sons, 2021.

[5] M. Montel, X-ray microscopy with catamegonic roof mirrors, X-ray Microscopy and Microradiography (1957) 177–185.

[6] C. Liu, G. E. Ice, W. Liu, L. Assoufid, J. Qian, B. Shi, R. Khachatryan, M. Wieczorek, P. Zschack, J. Z. Tischler, Fabrication of nested elliptical KB mirrors using profile coating for synchrotron radiation X-ray focusing, Applied Surface Science 258 (6) (2012) 2182–2186.

[7] K. Mundboth, J. Sutter, D. Laundy, S. Collins, S. Stoupin, Y. Shvyd'ko, Tests and characterization of a laterally graded multilayer Montel mirror, Synchrotron Radiation 21 (1) (2014) 16–23.

[8] B.-Y. Chen, G.-C. Yin, C.-Y. Lee, M.-Y. Hsu, B.-H. Lin, S.-C. Tseng, X.-Y. Li, H.-Y. Chen, J.-X. Wu, S.-H. Chang, et al., The Precise Adjustment of X-ray Montel Mirrors for Diffraction-Limited Focal Spots, Synchrotron Radiation News 31 (5) (2018) 27–32.

[9] G.-C. Yin, B.-Y. Chen, C.-Y. Lee, H.-Y. Chen, B.-H. Lin, S.-C. Tseng, X.-Y. Li, J.-X. Wu, S.-H. Chang, M.-T. Tang, Nanoprobe Endstation with Montel optics and Resolution 50 nm at Taiwan Photon Source, Microscopy and Microanalysis 24 (S2) (2018) 208–209.

[10] K. A. Goldberg, Derivation of closed-form ellipsoidal X-ray mirror shapes from Fermat's principle, Synchrotron Radiation 29 (4) (2022) 991–996.

[11] T. Wang, L. Huang, H. Choi, M. Vescovi, D. Kuhne, Y. Zhu, W. C. Pullen, X. Ke, D. W. Kim, Q. Kemao, et al., RISE: robust iterative surface extension for sub-nanometer X-ray mirror fabrication, Optics Express 29 (10) (2021) 15114–15132.

[12] T. Wang, L. Huang, Y. Zhu, S. Giorgio, P. Boccabella, N. Bouet, M. Idir, Ion beam figuring system for synchrotron x-ray mirrors achieving sub-0.2-μrad and sub-0.5-nm root mean square, Nanomanufacturing and Metrology 6 (1) (2023) 20.

[13] L. Huang, T. Wang, J. Nicolas, A. Vivo, F. Polack, M. Thomasset, C. Zuo, K. Tayabaly, D. Wook Kim, M. Idir, Two-dimensional stitching interferometry for self-calibration of high-order additive systematic errors, Optics Express 27 (19) (2019) 26940–26956.

[14] L. Huang, T. Wang, K. Tayabaly, D. Kuhne, W. Xu, W. Xu, M. Vescovi, M. Idir, Stitching interferometry for synchrotron mirror metrology at National Synchrotron Light Source II (NSLS-II), Optics and Lasers in Engineering 124 (2020) 105795.

[15] S. Qian, M. Idir, Innovative nano-accuracy surface profiler for sub-50 nrad rms mirror test, in: 8th International Symposium on Advanced Optical Manufacturing and Testing Technologies: Subnanometer Accuracy Measurement for Synchrotron Optics and X-Ray Optics, Vol. 9687, SPIE, 2016, pp. 81–90.

[16] L. Huang, L. Lienhard, T. Wang, F. Polack, J. Nicolas, S. Hulbert, M. Idir, Multi-pitch nano-accuracy surface profiler for strongly curved X-ray mirror metrology, Optics and Lasers in Engineering 162 (2023) 107428.

[17] T. Wang, L. Huang, M. Vescovi, D. Kuhne, Y. Zhu, V. S. Negi, Z. Zhang, C. Wang, X. Ke, H. Choi, et al., Universal dwell time optimization for deterministic optics fabrication, Optics express 29 (23) (2021) 38737–38757.

[18] T. Wang, X. Ke, L. Huang, Q. Cui, Z. Zhang, C. Wang, H. Kang, W. Pullen, H. Choi, D. Kim, V. Negi, Q. Kemao, Y. Zhu, S. Giorgio, N. Boccabella, Philip Bouet, C. Austin, M. Idir, A comprehensive review of dwell time optimization methods in computer-controlled optical surfacing, Light: Advanced Manufacturing 5 (2024) 422.

[19] X. Ke, J. Fan, T. Wang, L. Huang, Y. Zhu, C. Austin, H. Choi, H. Kang, V. Negi, D. Kim, et al., E-PVT: enhanced position-velocity-time scheduler for computer-controlled optical finishing with comprehensive considerations of dynamics constraints, continuity and efficiency, Optics Express 32 (9) (2024) 15507–15526.

[20] X. Xie, L. Zhou, Y. Dai, S. Li, Ion beam machining error control and correction for small scale optics, Applied Optics 50 (27) (2011) 5221–5227.

[21] M. D. Kriese, Y. Li, Y. Y. Platonov, High-precision MoSi multilayer coatings for radial and 2D designs on curved optics, in: International Conference on Extreme Ultraviolet Lithography 2017, Vol. 10450, SPIE, 2017, pp. 323–323.